 doi:10.20944/preprints202206.0043.v1

Article

LumbarNet: A Deep Learning Network for the Automated Detection of Lumbar Spondylolisthesis From X-Ray Images

Giam Minh Trinh[1,2,3], Hao-Chiang Shao[4], Kevin Li-Chun Hsieh[5,6,7], Ching-Yu Lee[8,9], Hsiao-Wei Liu[10], Chen-Wei Lai[10], Sen-Yi Chou[10], Pei-I Tsai[11], Kuan-Jen Chen[11], Fang-Chieh Chang[11], Meng-Huang Wu[8,9,12]* and Tsung-Jen Huang[8,9]*

1 International Ph.D. Program in Medicine, College of Medicine, Taipei Medical University, Taipei 11031, Taiwan
2 Department of Trauma-Orthopedics, College of Medicine, Pham Ngoc Thach Medical University, Ho Chi Minh city 700000, Vietnam
3 Hospital for Traumatology and Orthopedics, Ho Chi Minh city 700000, Vietnam; minhgiam1310@gmail.com
4 Department of Statistics and Information Science, Fu Jen Catholic University, New Taipei city 242062, Taiwan; shao.haochiang@gmail.com
5 Department of Medical Imaging, Taipei Medical University Hospital, Taipei 11031, Taiwan
6 Research Center of Translational Imaging, Taipei Medical University Hospital, Taipei 11031, Taiwan
7 Department of Radiology, College of Medicine, Taipei Medical University, Taipei 11031, Taiwan; Kevinh9396@gmail.com
8 Department of Orthopedics, College of Medicine, Taipei Medical University, Taipei 11031, Taiwan
9 Department of Orthopedics, Taipei Medical University Hospital, Taipei 11031, Taiwan; ejaca22@gmail.com (C.Y.L.)
10 Center for Measurement Standards, Industrial Technology Research Institute, Hsinchu 30044, Taiwan; rachel_liu@itri.org.tw (H.W.L.); ChenWeiLai@itri.org.tw (C.W.L.); senyih@itri.org.tw (S.Y.C.)
11 Biomedical Technology and Device Research Laboratories, Industrial Technology Research Institute, Hsinchu 31057, Taiwan; peiyi@itri.org.tw (P.I.T.); cgrchen@itri.org.tw (K.J.C.); funjay@itri.org.tw (F.C.C.)
12 TMU Biodesign Center, Taipei Medical University, Taipei 11031, Taiwan
* Correspondence: maxwutmu@tmu.edu.tw (M.H.W.); tjdhuang@tmu.edu.tw (T.J.H.) (These authors contributed equally to this work)

Abstract: A common spinal condition, spondylolisthesis is the presence of a relative back or forth displacement between the upper and lower vertebra due to one vertebra being oriented away from the smooth curvature of a normal spine. Degenerative spondylolisthesis usually occurs in the lumbar spine, especially at L4-L5, and is more prevalent among women aged older than 60 years. Aging-related illnesses such as degenerative spondylolisthesis are especially burdensome on social welfare and health-care systems in an aging society. Therefore, to address this issue, we proposed a computer aided diagnosis (CADx) algorithm, named LumbarNet, for vertebral slippage detection on clinical X-ray images. Collaborating with i) a P-grade, ii) a piecewise slope detection (PSD) scheme, and iii) a dynamic shift (DS) detection routine, LumbarNet was thus specialized for analyzing complex structural patterns in lumbar spine X-ray images (true lateral view, flexion and extension lateral view) and outcompeted other U-Net based methods. Extensive experiments on lumbar spine X-ray images in standard clinical practices showed that LumbarNet achieved a mean intersection over union (mIOU) value of 0.88 in vertebral region detection and an accuracy of 88.83% in vertebral slippage detection.

Keywords: deep learning, lumbarnet, lumbar spine, spondylolisthesis, u-net

1. Introduction

The human spine supports the central axis of the body and comprises 7 cervical vertebrae, 12 thoracic vertebrae, 5 lumbar vertebrae, 5 sacral vertebrae, and 4 coccygeal vertebrae. The lateral side of the spine presents a double-S-bend, which forms a physiological curvature along the neck, chest, abdomen and pelvis to provide flexibility during

 doi:10.20944/preprints202206.0043.v1

movement, including walking [1–3]. Spinal degenerative diseases often appear at the lower parts of the lumbar and cervical spine because these parts are subject to the highest dynamic and static forces [3,4]. The misalignment of lumbar vertebrae is a common deformity that makes the nerve roots to be pulled or compressed, causing low back pain, sciatica, or lower extremity pain and numbness. Consequently, it is clinically necessary for orthopedists or neurosurgeons to diagnose various spinal conditions including spinal fractures, scoliosis [5,6], spinal deformity [7], degenerative spondylolisthesis [8,9], stenosis [10,11], herniated intervertebral disc (HIVD) [12,13] and degenerative osteophytes [14]. According to AO (Arbeitsgemeinschaft für Osteosynthesefragen) spine founded in 1958 in Biel-Bienne, Switzerland by a group comprising Swiss general and orthopaedic surgeons, the annual global incidence of degenerative spine disease and spondylolisthesis are 3.63% and 0.53%, respectively [15].

Spondylolisthesis is the displacement of one vertebra on top of another [16–18]. It is termed anterolisthesis and retrolisthesis if a vetebra slips forward and backward relative to another, respectively [18,19]. Approximately 50%–81% of cases of spondylolisthesis result from lumbar spondylolysis [16]. Spondylolisthesis has a variety of etiologies, such as: hereditary factors, disc degeneration, and frequent engagement in lumbar activities involving repetitive hyperflexion and high rotation loads. Groups at high risk of developing spondylolisthesis include manual workers, weightlifters, gymnasts, dancers and football players [17,19]. Retrolisthesis has historically been considered an incidental finding that does not result in clinically significant symptoms. It appears in degenerative conditions, after injury, or in cases of adjacent segment disease. The detection of retrolisthesis from extension radiographs is relatively rare. The diagnosis rate reaches 30% among patients with chronic low back pain [20]. Computed tomography (CT), magnetic resonance imaging (MRI), and bone scans are useful for identifying the lesion site [17]. However, physicians usually recommend that lateral lumbar plain film radiographs in the flexion and extension views are used to assess spondylolisthesis and the degree of spinal instability. These radiographs offer quick results, are inexpensive, and can be easily obtained in a clinic or primary hospital. The Wiltse-Winter classification distinguishes spondylolisthesis into six types by etiology, with the most common being isthmic, degenerative, and dysplastic spondylolisthesis [17,19]. Spondylolisthesis, especially dysplastic or degenerative spondylolisthesis, can cause spinal canal stenosis, low back pain and leg pain, or neural compression symptoms [19,21]. Moreover, the Meyerding classification with 5 variants is widely used on clinical practice or research because this classification is simple to understand and easy to apply although it has some limitation in prognostic [19,22].

Surgery is the mainstay treatment method for patients who are dissatisfied with conservative management. However, it remains unclear whether the optimal surgical treatment is the use of decompression alone or the use of decompression in combination with either non-instrumented or instrumented fusion [23]. Hence, it is important to make a surgical plan and to predict the possibility of junctional failure or mechanical instability after surgery through a pre-operative recognition of spondylolisthesis. Moreover, with global population aging, spinal diseases are becoming increasingly prevalent. This growing prevalence is expected to place a greater strain on economies and health-care systems; in particular, physicians will have increased workloads in diagnosing spinal diseases. Sophisticated methods for automatically diagnosing spinal diseases are thus required.

Semantic segmentation algorithms are fundamental to object identification in medical images, such as those obtained using X-ray, MRI, and CT scanner images [12]. Segmentation, detection, and measurement performed using X-ray images are challenging due to the contrast and diversity in X-ray images, particularly with regard to the complexity of spinal structures. To the best of our knowledge, the present study is the first to construct a fully convolutional network for detecting spondylolisthesis from X-ray images. Based on U-Net and image measurement analysis technology, we hope to provide an automatic spondylolisthesis detection on X-ray images with high accuracy, low false-negative rate to reduce the misdiagnosis or subjective errors of the observers and plan for treatment

Preprints (www.preprints.org) | NOT PEER-REVIEWED | Posted: 3 June 2022 doi:10.20944/preprints202206.0043.v1

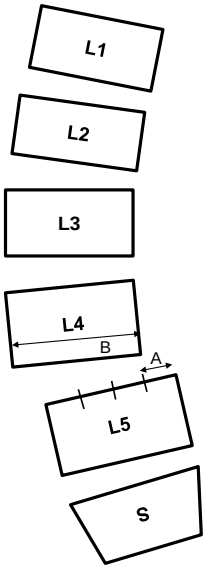

Figure 1. Schematic diagram of lumbar vertebrae and slippage judgement: L refers to lumbar vertebra, S refers to sacral vertebra; A is the slip distance between two vertebrae, and B is the width of the upper vertebra.

on clinical. In this study, we determined the threshold values (K values) that indicate the presence of vertebral slippage and evaluated the accuracy of our method.

Our study makes four primary contributions:

- This is the first study to address the problem of identifying lumbar slippage from single and paired X-ray images.
- LumbarNet is computationally efficient than U-Net based schemes. With the aids of spatial and content features, LumbarNet can achieves a state-of-the-art performance in lumbar and sacrum segmentation tasks.
- This study features a novel application of piecewise slope detection (PSD), dynamic shifting (DS), and the hybrid judgement of P-grade and PSD value to enhance slippage detection on the lumbar spine.
- Extensive experiments shows that our method is robust against the presence of sacral lumbolization phenomenon and reaches a high accuracy value accordingly.

The remainder of this paper is organized as follows. We review the literature in section 2. LumbarNet and algorithm for detecting spondylolisthesis are detailed in sections 3. Our experimental results are presented in section 4. Finally, we conclude the paper in section 5.

2. Related works

2.1. Spondylolisthesis

In spondylolisthesis diagnosis, the degree of slippage is classified into five grades by comparing the displacement extent of the superior vertebra with the equal four parts of the inferior vertebra. The quotient of the bare displacement value of the upper vertebra (A) and the width of the upper vertebra (B) is calculated to obtain a P-grade (as illustrated in Figure 1). Table 1 lists the relationship between the P-grade and the degree of vertebral splippage. By taking 50% as a border line, a P-grade that is less and more than 50% indicates mild and severe slippage, respectively. A P-grade greater than 100% represents a complete verebral slippage, the most serious condition [24].

2.2. Deep learning for semantic segmentation

Image segmentation method is used to divide a digital image into multiple elements or regions. Image segmentation is widely used in various fields, especially in medicine.

Preprints (www.preprints.org) | NOT PEER-REVIEWED | Posted: 3 June 2022 doi:10.20944/preprints202206.0043.v1

Table 1. Classification of the vertebral slippage degree.

P-grade (A/B)	%	Description
Grade 1	0-25 %	Low grade
Grade 2	25-50 %	
Grade 3	50-75 %	High grade
Grade 4	75-100 %	
Grade 5	Vertebral body completely fallen off	Spondyloptosis

The rapid development of machine learning in general and the emergence of deep neural networks in particular have accelerated advances in automated image recognition.

Convolutional neural networks (CNNs) yield large improvements in semantic segmentation [25–28]. Pixel wise labelling in an image is commonly executed when semantic segmentation is used. The main task of semantic segmentation is to identify the class labels in a pixel-by-pixel manner given the context of an image [25,29]. In medicine, this technique is typically applied to images of cancer cells, muscle tissue, the aortic wall, and bones [30].

Deep learning has recently been employed in various medical applications [31], but deep learning techniques in medicine (e.g., for segmentation, detection, and classification) have rarely been applied to the detection of lumbar lesions from X-ray images.

Formulated to detect the vertebrae by Lecron et al [32], the active shape model (ASM) segments X-ray images of vertebrae by using edge polygon approximation techniques. Although the ASM method exhibits favorable efficiency in experiments, its execution time and applicability to clinical contexts remain areas of concern. Therefore, authors proposed a parallel hybrid implementation in which vertebral features are extracted using the power of multiple graphics processing units (GPUs) or central processing units running in parallel to enhance performance.

Ronneberger et al formulated U-Net, an end-to-end training network that contains an encoder–decoder network structure and has a symmetrical U-shaped structure that uses paired primitives and markers during training. The model is then trained by U-Net to process a cellular image to output a binary map. U-Net is characterized by superior training performance on data sets covering a small set of examples and it achieved an accuracy of up to 92% in an experiment with medical images (512 x 512 in resolution) when executed using GPU acceleration [33].

Kuok et al used U-Net to determine the region of interest (ROI) in anteroposterior X-ray images of the entire spine. Specifically, they first extracted and enhanced the images before applying intensity horizontal and vertical projections to obtain projection histograms. The trained model had a minibatch size of 30, and the learning rate was set to 1. The L2 loss function was employed, and the cross validation method was used in the experiments. The dice similarity coefficient (DSC) of the X-ray images was 94.1% in the experiment [34].

Konya et al trained a model on 730 X-ray images of the lateral lumbar spine by using deep neural networks. Their workflow, from start to finish, comprised data retrieval, data preparation, model training, model output, and analysis [35]. Various methods, such as U-Net [33], Mask R-CNN [36,37], PSPNet [38], DeepLabV3 [39], and YOLACT [40], were implemented. That study adopted four indexes of accuracy: the pixel accuracy average, mean intersection over union (IOU) average, mean accuracy average, and frequency weighted IOU average. Both U-Net and YOLACT exhibited favorable segmentation performance. The inference results demonstrated that these methods support decision-making for further processing pipelines.

With regard to the measurement of the critical value for lumbar vertebrae, Cho et al developed a machine learning and computer vision based method for measuring the extent of a lumbar lordosis (LL) from radiological images. In that study, 780 lateral X-ray images were used for training, testing, and data augmentation with respect to improving contrast,

Preprints (www.preprints.org) | NOT PEER-REVIEWED | Posted: 3 June 2022 doi:10.20944/preprints202206.0043.v1

and intensity normalization was performed to synthetically generate 12,580 images for training. In experiments, U-Net segmentation achieved a dice score of 0.821 and a mean absolute error for LL of 8.055° [41].

2.3. Improving the accuracy of U-net

The U-Net architecture does not have any fully connected layers. Furthermore, only the verification part of each convolution is used; this allows the segmentation map to contain each pixel of the input image in its full context. In addition, the application of U-Net likes a mask purpose for two groups of segmented region, with one being the foreground and the other being the background. SegNet with a pixel wise classification layer was proposed to obtain more accurate semantic segmentation results. SegNet has favorable efficiency because it saves the max-pooling indexes of feature maps in its decoder network. However, both efficiency and accuracy are key in semantic segmentation, and this necessitates improvements to pixelwise segmentation [42]. The feature fusion architecture was first used in a feature fusion single-shot multi box detector (FSSD). The feature fusion module generates detailed feature maps in the object detection part [43]. A bilateral segmentation network which has two-path architecture comprising a spatial path and a context path, was constructed by Yu [44], [45]. The spatial path could preserve the spatial information of original images. In experiments, the network achieved a result of 105 frames per second (FPS) on the Cityscapes data set, which contains images with a resolution of 1024 x 2048. Drawing on these studies in the literature, the present study formulated a deep learning method that combines U-Net, feature fusion models, and various image processing techniques to detect abnormal slippage in clinical medical images.

3. Materials and Methods

3.1. LumbarNet for segmenting vertebral regions from X-ray images

Each lumbar vertebrae and sacrum region on X-ray images should be segmented in the detection of lumbar slippage. In traditional image processing, either the binarization method with a determined threshold or an automatic binary method, such as Otsu, adaptive method. However, the ROIs obtained using the binarization method are greatly influenced by the distribution of grayscale values in the foreground and the background. Owning to diverse contrasts from X-ray images, this study formulated LumbarNet, a deep convolution neural networks, instead of using traditional computer vision methods. LumbarNet is a semantic segmentation network that facilitates the understanding of lumbar X-ray images in machine learning. U-Net, used in medical image segmentation, structurally comprises two convolutional networks paths: a contraction path, and an expansion path called the encoder and decoder, respectively. The contraction path functions to extract features from the input image, and the expansion path functions up samples the extracted features and generates the segmented image in comparison with the input image. To improve the encoder 's efficiency, we added the feature fusion model (FFM) to the encoder path. The FFM module comprised convolutional layers with a stride function, batch normalization and rectified linear unit (ReLU) activation functions, average pooling layers, add operators, and a multiply operator. Figure 2 details the schema of LumbarNet, including the encoder types, decoder type, and FFM. The input layer of LumbarNet has a size of 512 x 512 x 3, and the FFM model is a feature fusion model composed of convolution and by batch normalization and ReLU combinations.

The LumbarNet model uses a pixel wise softmax function to calculate the loss function, and the cross entropy loss is defined follows:

$$E = -\sum_{i=1}^{n} w(x) log p(x) \quad (1)$$

By classifying each pixel as an end-to-end image for learning and output, the inference and image processing operations of LumbarNet are executed according to the following procedure to confirm whether a patient has spondylolisthesis.

Preprints (www.preprints.org) | NOT PEER-REVIEWED | Posted: 3 June 2022 doi:10.20944/preprints202206.0043.v1

Encoder Type	Encoder Kernel size/stride	Encoder Output size	Decoder Type	Decoder Kernel size/ stride	Decoder Output size
Conv1 + relu	3x3/1	512x512x32	UpConv1	2x2	32x32x1024
Conv2 + relu	3x3/1	512x512x32	Conv1+Relu	2x2/1	32x32x512
MaxPooling	2x2/2	256x256x32	Concatenate (Conv1 + relu, Dropout1)		
Conv3 + relu	3x3/1	256x256x64	Conv2+relu	3x3/1	32x32x512
Conv4 + relu	3x3/1	256x256x64	Conv3+Relu	3x3/1	32x32x512
MaxPooling	2x2/2	128x128x64	UpConv2	2x2	64x64x512
Conv7 + relu	3x3/1	64x64x256	Conv4+relu	3x3/1	64x64x256
Conv8 + relu	3x3/1	64x64x256	UpConv3	2x2	128x128x256
MaxPooling	2x2/2	32x32x256	Conv5+relu	3x3/1	128x128x128
Conv9	3x3/1	32x32x512	Concatenate (Conv5 + relu, Conv6+relu)		
Conv10+relu	3x3/1	32x32x512	Conv7 + relu	3x3/1	128x128x128
Dropout(0.5)			Conv8 + relu	3x3/1	128x128x128
MaxPooling	2x2/1	16x16x512	UpConv4	2x2/1	256x256x128
Conv11+relu	3x3/1	16x16x1024	Conv9+relu	3x3/1	256x256x64
Conv12+relu	3x3/1	16x16x1024	Concatenate(Conv9+relu, Conv10+relu)		
Dropout(0.5)			Conv11+relu	3x3/1	256x256x64
Fusion Feature Model (FFM)			Conv12+relu	3x3/1	256x256x64
FFM Type	**FFM Kernel size/stride**	**FFM Output Size**	UpConv5	2x2	512x512x64
Cov1	32x32/2	256x256x32	Conv6+relu	3x3/1	512x512x32
BatchNorm1+Relu		256x256x32	Concatenate (Conv6+relu, Conv7+relu)		
Conv2	64x64/2	256x256x32	Conv8+relu	3x3/1	512x512x32
BatchNorm2+Relu		Conv9+relu	3x3/1	512x512x32	
Conv3	156x156/2	64x64x156	Conv10+relu	3x3/1	512x512x5
BatchNorm3 +Relu		64x64x156			
Concatenate (Batch-Norm3+Relu, Conv4)		64x64x412			
Conv5	3x3/1	64x64x4			
BatchNorm4+Relu		64x64x4			
AveragePooling	2x2/1	64x64x4			
Conv6+Relu	1x1/1	64x64x4			
Conv7+Sigmoid	1x1/1	64x64x4			
Multiply (Conv7+Sigmoid, BatchNorm4+Relu)		64x64x4			
Add (Multiply, NatchNorm4+Relu)		64x64x4			

Figure 2. Architecture of LumbarNet.

3.2. Detection of lumbar spondylolisthesis

The original image is resized to 512 x 512 pixels, and LumbarNet is used and applied to the resized image. Subsequently, the segmented image is generated using by the output of LumbarNet. The nearest-neighbor interpolation method is then applied to scale the segmented image to the original image 's size. The segmented image has three labels: the background, vertebral regions, and the sacrum. Thereafter, ROIs on the labeled image could be extracted using the contour finding method. Through the use of a method based on eight connected components, each vertebral region and sacrum region can be detected. Finally, the fitted quadrilateral of the vertebral region is calculated using a pole.

3.2.1. P-grade

There are five lumbar vertebrae in total. The quadrilateral of each vertebra L_i has four extreme points, where $i \in \{1, 2, 3, 4, 5\}$. The upper-left point of a lumbar vertebra L_i is $p_{L_{i,1}}$, the upper-right point of lumbar vertebra L_i is $p_{L_{i,2}}$, the lower-right point of lumbar vertebra L_i is $p_{L_{i,3}}$, the lower-left point of lumbar vertebra L_i is $p_{L_{i,4}}$. The sequence of four points of each vertebra runs counterclockwise from the upper-left point. In addition, the top plate of

Preprints (www.preprints.org) | NOT PEER-REVIEWED | Posted: 3 June 2022 doi:10.20944/preprints202206.0043.v1

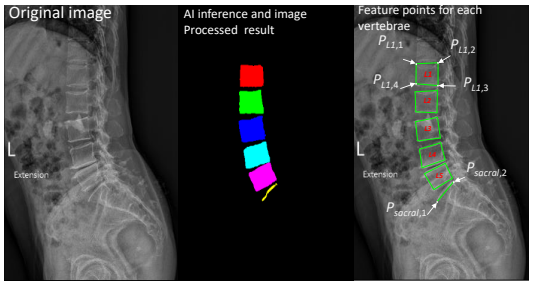

Figure 3. Original image, processed image, and calculated feature points of each vertebrae and sacrum.

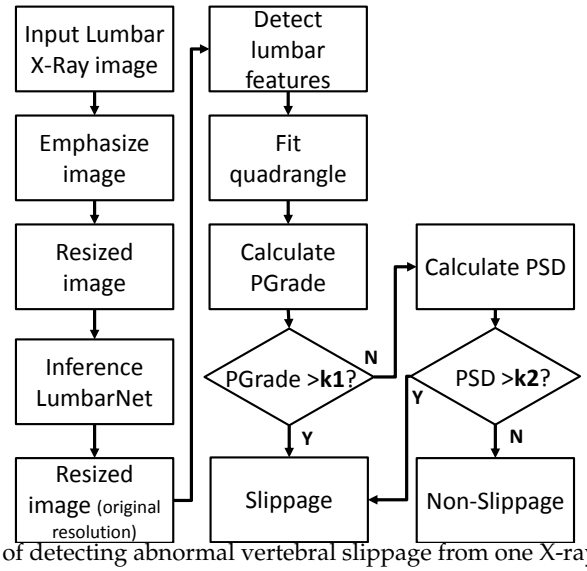

Figure 4. Process of detecting abnormal vertebral slippage from one X-ray image by using P-grade.

the sacrum represented by two points, namely the left and right points p_{sacral_1} and p_{sacral_2}, respectively, of the upper plate of the vertebral plate, as illustrated in Figure 3.

After these feature points are detected, P-grade for the difference between the left and right vetebral segments is calculated, with values >20% indicating abnormality. The process of such a determination of abnormality from one X-ray image is illustrated in Figure 4. Each P-grade, specifically that corresponding to L1-L2, L2-L3, L3-L4, L4-L5, and L5-S1, is calculated, and the algorithm checks whether the P-grade is greater than K_1, as indicated in the following equations:

$$f_{pgrade}(m,n) = p_{grade}(i,j) > K_1, \tag{2}$$

$$p_{grade}(i,j) = \frac{D(P_{i,proj}, P_{j,2})}{\sqrt{\|P_{j,1} - P_{j,2}\|^2}}, \tag{3}$$

$$D(P_{i,proj}, P_{j,2}) = \sqrt{\|P_{i,proj} - p_{j,2}\|^2}. \tag{4}$$

where f_{pgrade} is the shift value of the lower plate of the i-th lumbar vertebrae relative to the upper plate of the the j-th lumbar vertebrae. Both i and j are indexes for the proximal vertebral regions, specifically $i \in \{L1, L2, L3, L4, L5\}$ and $j \in \{L2, L3, L4, L5, S1\}$. Subsequently, the algorithm determines the projected point p_{proj} between the point $p_{i,3}$ and line L_j, the end points of which are $p_{j,1}$ and $p_{j,2}$, is measured. Thereafter, the distance $D_{p_{i,3},L_j}$ between the projected point and upper right point, $p_{j,2}$, of the j-th lumbar vertebra is computed. In addition, f_{pgrade} is computed by dividing $D(P_{i,proj}, P_{j,2})$ by the length of upper plate of the j-th lumbar vertebra, as illustrated in Figure 5. The projected point is

Preprints (www.preprints.org) | NOT PEER-REVIEWED | Posted: 3 June 2022 doi:10.20944/preprints202206.0043.v1

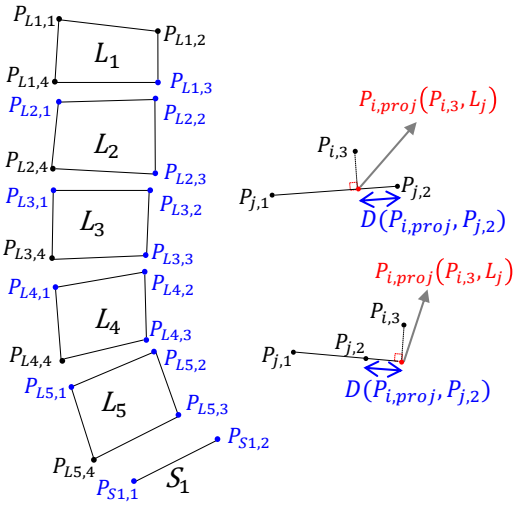

Figure 5. Five lumbar vertebrae with four points, and a sacrum with two points. Projected point may lie either within or beyond the segmented line.

either within or beyond the segmented line, which marks the upper plate of the j-th lumbar vertebrae.

3.2.2. Piecewise slope detection (PSD)

Because each lumbar vertebra has the extreme points: $p_{L_{i,1}}$, $p_{L_{i,2}}$, $p_{L_{i,3}}$, and $p_{L_{i,4}}$. The vertical shift angle is measured and used to directly detect the variation in the angle between the proximal lumbar region and its gap. The angle θ is calculated using the cosine theorem for the gap between the upper and lower points and the corresponding vertical line. Because splippage of the lumbar vertebrae is present in anterolisthesis and retrolisthesis, both the left and right sides of the lumbar vertebrae are considered in the calculation of the degree. Specifically, the angles θ_α and θ_β correspond to the left and right sides of each vertebra, respectively. The subscripted α and β correspond to the detection of the difference in the slope for the left and right vertebral segments, respectively. The PSD method detects slippage using the following equations:

$$f_{slippage}(m,n) = |\theta_{i,j} - \theta_{i,j+1}| > K2, \tag{5}$$

$$\theta_{(i,j)} = \cos^{-1} \frac{\vec{U} \cdot \vec{V}}{\|U\| \times \|V\|}, \tag{6}$$

where $i \in \{\alpha, \beta\}$, $j \in \{1,2,...,10\}$, and (m,n) is for the proximal vertebrae from L_1 to S_1 and is in adjacent paired regions. If (m,n) equals to (L_1, L_2), then slippage might be present between the first and second lumbar vertebrae for any j = 1, 2, and 3. If (m,n) equals to (L_5, S_1), then slippage might be present between the fifth lumbar and sacrum for any j = 9 and 10. Each θ is computed using Eq. (6), where U is a vector for two consecutive points on a segment and V represents the vertical points. Each point and segment of the first and second lumbar vertebra are detailed in Figure 6.

3.2.3. Dynamic shift (DS) detection

DS detection is applied to two X-ray images in the flexion and extension positions to calculate the shift in the proximal lumbar region when the patient leans forward and backward. The procedure for DS detection is illustrated in Figure 7.

Similarly, Eq. (4) is used to calculate the shift in the proximal lumbar region and f_{ds} is used to check whether the shift distance is greater than $K3$. The formula is as follows:

$$f_{ds}(i,j) = |D(P_{i,proj}, P_{j,2}) - D^{'}(P^{'}_{i,proj}, P^{'}_{j,2})| > K3, \tag{7}$$

Preprints (www.preprints.org) | NOT PEER-REVIEWED | Posted: 3 June 2022 doi:10.20944/preprints202206.0043.v1

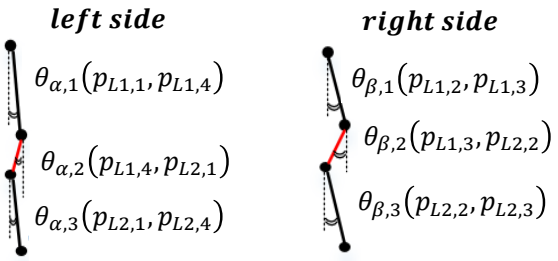

Figure 6. Descriptions of each angle of PSD methodology. There are four extreme points of each lumbar vertebra. $p_{Li,1}$, $p_{Li,2}$, $p_{Li,3}$, and $p_{Li,4}$, which respectively correspond to the upper-left point, upper-right point, lower-right point, and lower-left point of a lumbar vertebra i. Each vertebral region can be calculated the left- and right-side angles between proximal line segments. θ_α stands for the left side and θ_β stand for the right side.

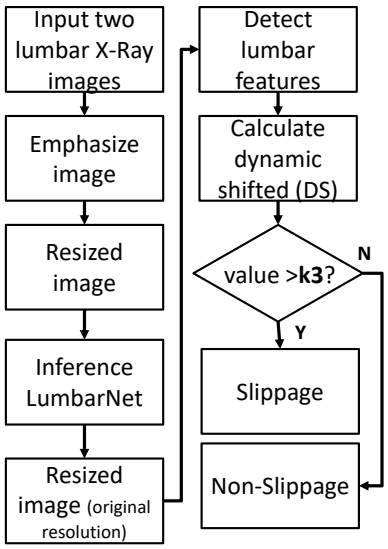

Figure 7. Process of detecting abnormal vertebral slippage from flexion and extension X-ray images by using dynamic shift detection.

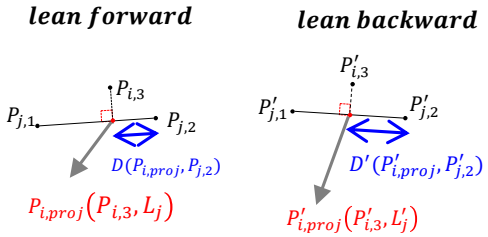

Figure 8. Illustration of dynamic shift for slippage detection.

where $D(P_{i,proj}, P_{j,2})$ and $D'(P'_{i,proj}, P'_{j,2})$ are shift distances from leaning forward and backward, respectively, each determined from separate X-ray images as illustrated in Figure 8. The index $i \in \{\text{L1, L2,L3, L4, L5}\}$, and the index $j \in \{\text{L2, L3,L4, L5, S1}\}$. If the patient only has one X-ray image, the P-grade and PSD methods are executed. However, if the patient has more than two X-ray images, the P-grade, PSD, and DS methods are executed in sequence for spondylolisthesis diagnosis.

Preprints (www.preprints.org) | NOT PEER-REVIEWED | Posted: 3 June 2022 doi:10.20944/preprints202206.0043.v1

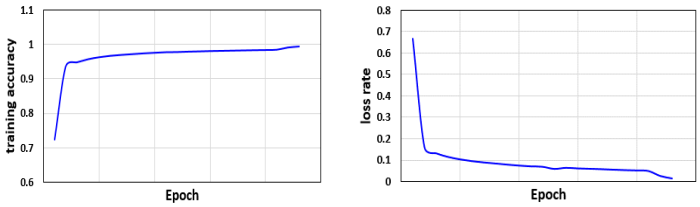

(a): accuracy (b): loss function

Figure 9. Training history of LumbarNet.

4. Results and discussion

4.1. Data set

In this research, the lumbar X-ray images were captured by the X-ray machine (Radnext 50, Hitachi Global, Tokyo, Japan). The patients were required to either stand up or lean forward and backward. After full IRB approval was granted (TMU-JIRB No.: N201807084), 706 X-ray images of patients having low back pain were collected at Taipei Medical University Hospital by radiologists. Although the images were taken under the same X-ray settings (including the same X-ray energy), the generated digital images differed greatly in contrast and grayscale range. The vertebral and sacral regions on these images were manually labeled. The extent slippage in each vertebrae image were scored by two orthopedists. We expanded our data set through data augmentation using transformations such as rotation, changes in contrast, and flipping. The images ranged widely in resolution from 494 to 2456 pixels in width and from 888 to 3408 pixels in height. Our model was applied to 312 X-ray images of abnormalities in lumbar vertebrae, with 250 and 62 images comprising the training and test sets, respectively. In the training model, the learning rate was $1e-4$, the Adam optimizer was used, the training period was 200 epochs, and the loss function was calculated per Eq.1.

The training accuracy was determined for each epoch, and the loss function is illustrated in Figure 9. Training and evaluation took 16 hours and 30 ms, respectively, on a Nvidia GTX 1080 Ti GPU. The accuracy reached 99.49% during the training phase. We then verified whether the learned geometric region intersected the artificially labeled ROIs by applying the learned model to the testing set to calculate mean intersection over union (mIOU). A true positive was indicated by each rectangular IOU probability being greater than 0.5. For U-Net, its mIOU was 0.8 and the mIOU values for L1, L2, L3, L4, L5, and the sacral regions were 0.76, 0.89, 0.83, 0.75, 0.76 and 0.83, respectively. For LumbarNet, its mIOU was 0.88 and the mIOU values for L1, L2, L3, L4, L5, and the sacral regions were 0.852, 0.889, 0.889, 0.889, 0.889 and 0.889, respectively (Table 2).

Table 2. mIOU Comparison of U-Net and LumbarNet.

$mIOU_{0.5}$	L1	L2	L3	L4	L5	Sacrum	Average
U-NET	0.76	0.89	0.83	0.75	0.76	0.83	0.8
LumbarNet	0.852	0.889	0.889	0.889	0.889	0.889	0.88

 doi:10.20944/preprints202206.0043.v1

4.2. Analytical experiments

4.2.1. K1 experiments for P-grade

The relationship between the bare displacement value A of the lower vertebra and the width B of the upper vertebra is calculated, as follows:

$$P\ grade = A/B \times 100 \tag{8}$$

Vertebral slippage, between the projected point and the upper-right point (pj,2) of the j-th lumbar vertebra was calculated. The shifted identification algorithm was applied to 394 cases for training, and a threshold value of K1 = 10 was suggested during training. The accuracy, sensitivity, specificity, false positive rate, and false negative rate were 88.05% (95% CI, 80%–91%), 89.44% (95% CI, 79%–94%), 84.92% (95% CI, 81%–86%), 7.32% (95% CI, 4%–6%) and 4.63% (95% CI, 4%–15%), respectively.

4.2.2. K2 experiments for PSD

In this chapter, the K value in the vertebral anomaly test algorithm was tested according to the samples and the better value of K was tested. In general, a larger K value indicates a greater allowable displacement between the upper and lower vertebrae. The K value was tested in 100 test points in sequence, and model performance was determined in terms of by precision and false positive rate. The test points were from all images, and the model results were tested against the judgment of orthopedists with regard to the location of vertebral slippage. A higher and lower K value correspond to a smaller and larger allowance, respectively, with respect to the accuracy and false positive rate. A K value of 37 was selected as the parameter of the subsequent slip abnormality detection. The accuracy, sensitivity, specificity, false positive rate, and false negative rate were 81.22% (95% CI, 75%–90%), 85.82% (95% CI, 81%–92%), 71.43% (95% CI, 61%–90%), 9.14% (95% CI, 4%–12%) and 9.64% (95% CI, 5%–13%), respectively.

4.2.3. K3 experiments for DS

The DS method was applied to X-ray images of the patient leaning forward and backward. If the difference between the shift distances for the forward and backward motions was greater than K3, spondylolysthesis was indicated. The final value of K3 was 0.14. Our trained model had an accuracy, sensitivity, specificity, false positive rate and false negative rate of 81.42% (95% CI, 80%–82%), 82.5% (95% CI, 79%–83%), 80.31% (95% CI, 79%–81%), 9.67% (95% CI, 9%-10%) and 8.91% (95% CI, 8%-10%), respectively.

The thresholds of K values are indicated in Figure 10. Furthermore, the combination of P-grade (K1=10) and PSD (K2=50) methods yielded the optimal results (Table 3), as indicated by an accuracy of 88.83% (95% CI, 84%–91%), sensitivity of 91.24% (95% CI, 85%–93%), specificity of 83.33% (95% CI, 81%–84%), false positive rate of 5.08% (95% CI, 4%–6%), false negative rate of 6.09% (95% CI, 5%–11%).

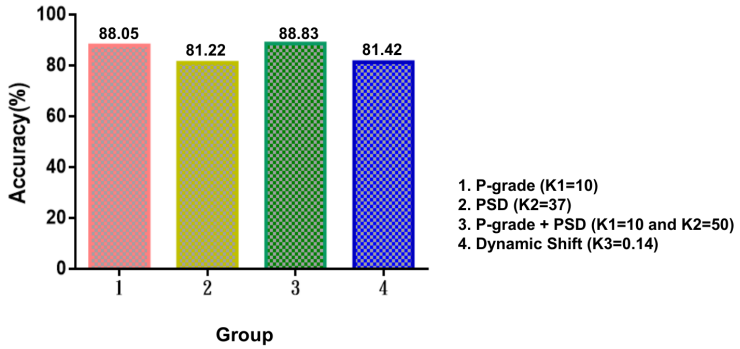

Figure 10. Accuracy of algorithm in different condition: P grade, Piecewise slope detection (PSD), Dynamic shift (DS).

Preprints (www.preprints.org) | NOT PEER-REVIEWED | Posted: 3 June 2022 doi:10.20944/preprints202206.0043.v1

Table 3. Accuracy, sensitivity, specificity, false positive rate, and false negative rate for spondylolisthesis detection.

	P-grade (K1=10)	PSD (K2=37)	P-grade+PSD (K1=10+K2=50)	DS (K3=0.14)
Accuracy	88.05% (95%CI, 80% − 91%)	81.22% (95%CI, 75% − 90%)	88.83% (95%CI, 84% − 91%)	81.42% (95%CI, 80% − 82%)
Sensitivity	89.44% (95%CI, 79% − 94%)	85.82% (95%CI, 81% − 92%)	91.24% (95%CI, 85% − 93%)	82.50% (95%CI, 79% − 83%)
Specificity	84.92% (95%CI, 81% − 86%)	71.43% (95%CI, 61% − 90%)	83.33% (95%CI, 81% − 84%)	80.31% (95%CI, 79% − 81%)
False positive	4.63% (95%CI, 4% − 6%)	9.14% (95%CI, 4% − 12%)	5.08% (95%CI, 4% − 6%)	7.67% (95%CI, 9% − 10%)
False negative	7.32% (95%CI, 4% − 15%)	9.64% (95%CI, 5% − 13%)	6.09% (95%CI, 5% − 11%)	8.91% (95%CI, 8% − 10%)

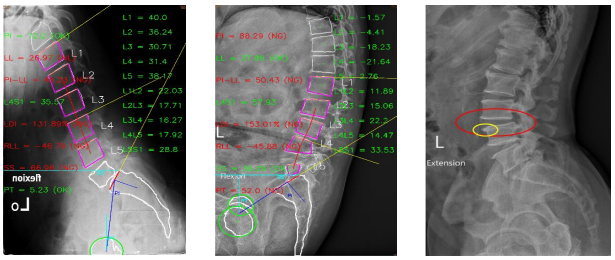

Figure 11. Errors in processing related to (a) poor lumbar image quality and overlap between the pelvis and vertebrae, (b) osteoporosis and lumbarsacralization, and (c) vertebral spurs.

Our results are similar to those of other studies on applying machine learning to detect spinal pathologies. Specifically, the faster adversarial recognition (FAR) network of Zhao et al for grading spondylolisthesis exhibited high accuracy (0.9883 ± 0.0094 in training, 0.8933 ± 0.0276 in testing) when used for the detection of vertebral abnormalities critical vertebrae in the absence of landmarks [46]. Furthermore, Ansari et al reported a high accuracy of 92.05% for their generalized regression network, which outperformed a neural network and support vector machine (SVM); their method was used to classify suspected spinal pathologies into healthy spine, disk hernia, and spondylolisthesis categories[47]. In addition, Karabulut et al reported a high accuracy of 89.73% for their synthetic minority oversampling technique (SMOTE), which is used for automatical classification and helped to make the right management for patients [48]. Finally, Akben reported a success rate of 84.5% for their naive Bayes classifier when it was used with a combination of three or more attributes. Akben also reported a 96.13% accuracy rate for their method in spondylolisthesis diagnosis, but he thought that this rate was misleadingly high because their samples were of unequal size [49].

Nonetheless, our accuracy rates are lower than those of Unal et al [50]. By combining a fuzzy C-means (FCM) algorithm with a naive Bayes classifier or SVM, they achieved high accuracy rates of 97.42% and 96.45%, which were substantially higher than the 82% to 85% achieved using the SVM [51]. Moreover, our study had some limitations. First, in our study, two orthopedists independently reviewed and confirmed spondylolisthesis but we didn't analyze the significance in interobserver and intraobserver differences. Second, we did not specify the spondylolysis and the slippage grade of spondylolisthesis on X-ray images because the aim of our study is spondylolisthesis detection to reduce the misdiagnosis for physicians on clinical and help to make planning for surgery. Furthermore, spinal anatomy is highly complicated complex, with many interconnected or overlapping structures. Therefore, lesion identification is more difficult in cases of osteoporosis, degenerative

 doi:10.20944/preprints202206.0043.v1

spine disease, or lumbarsacralization. Poor-quality X-ray images may also hinder lesion identification. These factors compromised the experimental performance of our method (as illustrated in Figure 11).

5. Conclusions

We formulated and evaluated LumbarNet, a U-Net based network. In experiments, it achieved an mIOU of up to 0.88 when determining the affected vertebral region. The ROI is then used to determine the end points, and slippage among the lumbar vertebrae is detected using the P-grade and PSD methods, which achieved an accuracy rate of 88.83% in experiments. Advances in medical imaging diagnosis are hampered by difficulties in collecting patient data, which requires ethical board approval. In addition, it needs to increase the experience and technical discussion in the professional field, and the number of cases can still be collected and verified continuously. Let the AI model and algorithm have more information to adjust. Future studies should focus on (1) strengthening the U-Net AI cutting model, and (2) increasing the physical quantity common to the physician's clinical diagnosis, such as the pelvic incidence (PI) or lumbar lordosis (LL) to increase the diagnosis of lumbar vertebral abnormalities such as vertebral fracture, herniated intervertebral disc (HIVD), lumbar spinal stenosis or spinal metastasis.

Author Contributions: Conceptualization, H.-C.S., H.-W.L., P.-I.T., M.-H.W.; methodology, G.M.T., H.-C.S., H.-W.L., M.-H.W.; software, H.-W.L., C.-W.L., K.-J.C., F.-C.C.; validation, K.L.-C.H., C.-Y.L., C.-W.L., M.-H.W.; formal analysis, G.M.T., H.-C.S., H.-W.L., C.-W.L.,S.-Y.C., P.-I.T., M.-H.W., T.-J.H.; investigation, M.-H.W., T.-J.H.; resources, K.L.-C.H., C.-Y.L.; data curation, G.M.T., H.-C.S., K.L.-C.H., C.-Y.L., H.-W.L., C.-W.L., M.-H.W., T.-J.H.; writing original draft preparation, G.M.T., H.-W.L., C.-W.L.; writing review and editing, G.M.T., H.-C.S., C.-W.L., M.-H.W.; visualization, H.-C.S., M.-H.W., T.-J.H.; supervision, H.-C.S., M.-H.W., T.-J.H.; project administration, S.-Y.C., P.-I.T., M.-H.W., T.-J.H.; funding acquisition, S.-Y.C., P.-I.T., M.-H.W.

Funding: This work was financially supported of the Higher Education Sprout Project by the Ministry of Education (MOE) (DP2-110-21121-01-A-14) and Industrial Technology Research Institute (ITRI) (L301ARE421) in Taiwan.

Institutional Review Board Statement: The Ethics Committee of Taipei Medical University Hospital (TMU-JIRB No.: N201807084) granted the ethics approval for the X-ray data collection.

Acknowledgments: The authors specially thank Mr. Hon-Pan Yiu, Research Assistant, Department of Orthopedics, College of Medicine, Taipei Medical University, Taipei, Taiwan for their helpful advice regarding the performance of this study.

Conflicts of Interest: The authors declare that they have no conflict of interests.

References

1. Cramer, G.D.; Darby, S.A. Clinical anatomy of the spine, spinal cord, and ANS-e-book **2017**.
2. Zubrzycki, J. Numerical analysis of spinal stabiliser in spondylolisthesis treatment with pedicle screws. *EDP Sciences. (2019)* **2017**, *252*.
3. Sąsiadek, M.J.; Bladowska, J. Imaging of degenerative spine disease the state of the art. *Advances in Clinical and Experimental Medicine* **2012**, *21*, 133–42.
4. Gallucci, M.; Limbucci, N.; Paonessa, A.; Splendiani, A. Degenerative disease of the spine. *Neuroimaging Clinics of North America* **2007**, *17*, 87–103.
5. Sabri, N.; Hamed, H.N.A.; Ibrahim, Z.; Ibrahim, K. 2D Photogrammetry Image of Scoliosis Lenke Type Classification Using Deep Learning. In Proceedings of the 2019 IEEE 9th International Conference on System Engineering and Technology (ICSET). IEEE, 2019, pp. 437–440.
6. Wu, H.; Bailey, C.; Rasoulinejad, P.; Li, S. Automated comprehensive adolescent idiopathic scoliosis assessment using MVC-Net. *Medical image analysis* **2018**, *48*, 1–11.
7. Glassman, S.D.; Bridwell, K.; Dimar, J.R.; Horton, W.; Berven, S.; Schwab, F. The impact of positive sagittal balance in adult spinal deformity. *Spine* **2005**, *30*, 2024–2029.
8. Jeon, I.; Kim, S.W. Retrolisthesis as a compensatory mechanism in degenerative lumbar spine. *Journal of Korean Neurosurgical Society* **2015**, *57*, 178.

9. Kawchuk, G.; Guan, R.; Keen, C.; Hauer, B.; Kondrak, G. Using artificial intelligence algorithms to identify existing knowledge within the back pain literature. *European Spine Journal: Official Publication of the European Spine Society, the European Spinal Deformity Society, and the European Section of the Cervical Spine Research Society* **2020**.
10. Khan, S.; Cloud, G.; Kerry, S.; Markus, H.S. Imaging of vertebral artery stenosis: a systematic review. *Journal of Neurology, Neurosurgery & Psychiatry* **2007**, *78*, 1218–1225.
11. Wu, X.; Zhao, Y.; Radev, D.; Malhotra, A. Identification of patients with carotid stenosis using natural language processing. *Imaging Informatics and Artificial Intelligence* **2020**, *30*, 4125–4133.
12. Oktay, A.B.; Akgul, Y.S. Diagnosis of degenerative intervertebral disc disease with deep networks and SVM. In Proceedings of the International Symposium on Computer and Information Sciences. Springer, 2016, pp. 253–261.
13. Salehi, E.; Khanbare, S.; Yousefi, H.; Sharpasand, H.; Sojoodi Sheyjani, O. Deep Convolutional Neural Networks for Automated Diagnosis of Disc Herniation on Axial MRI. In Proceedings of the 2019 Scientific Meeting on Electrical-Electronics Biomedical Engineering and Computer Science (EBBT), 2019, pp. 1–6.
14. Wang, Y.; J., Y.; Burns, J.; Liu, J.; Summers, R.M. Detection of Degenerative Osteophytes of the Spine on PET/CT Using Region-Based Convolutional Neural Networks. *4th International Workshop and Challenge, CSI 2016: International Workshop on Computational Methods and Clinical Applications for Spine Imaging* **2016**, pp. 116–124.
15. Ravindra, V.M.; Senglaub, S.S.; Rattani, A.; Dewan, M.C.; Härtl, R.; Bisson, E.; Park, K.B.; Shrime, M.G. Degenerative lumbar spine disease: estimating global incidence and worldwide volume. *Global spine journal* **2018**, *8*, 784–794.
16. McNeely, M.L.; Torrance, G.; Magee, D. A systematic review of physiotherapy for spondylolysis and spondylolisthesis. *Manual therapy* **2003**, *8*, 80–91.
17. Cavalier, R.; Herman, M.J.; Cheung, E.V.; Pizzutillo, P.D. Spondylolysis and spondylolisthesis in children and adolescents: I. Diagnosis, natural history, and nonsurgical management. *JAAOS-Journal of the American Academy of Orthopaedic Surgeons* **2006**, *14*, 417–424.
18. Jeon, C.; Park, J.; Chung, N.; Son, K.; Lee, Y.; Kim, J. Degenerative retrolisthesis: Is it a compensatory mechanism for sagittal imbalance? *The bone & joint journal* **2013**, *95*, 1244–1249.
19. Burke, C.J.; Shah, D.; Saha, S.; Houghton, R. Spondylolisthesis: a pictorial review. *British Journal of Hospital Medicine* **2012**, *73*, 691–695.
20. Shen, M.; Razi, A.; Lurie, J.D.; Hanscom, B.; Weinstein, J. Retrolisthesis and lumbar disc herniation: a preoperative assessment of patient function. *The Spine Journal* **2007**, *7*, 406–413.
21. Iguchi, T.; Wakami, T.; Kurihara, A.; Kasahara, K.; Yoshiya, S.; Nishida, K. Lumbar multilevel degenerative spondylolisthesis: radiological evaluation and factors related to anterolisthesis and retrolisthesis. *Clinical Spine Surgery* **2002**, *15*, 93–99.
22. Koslosky, E.; Gendelberg, D. Classification in Brief: The Meyerding classification system of spondylolisthesis. *Clinical orthopaedics and related research* **2020**, *478*, 1125.
23. Lubelski, D.; Alentado, V.J.; Williams, S.K.; O'Rourke, C.; Obuchowski, N.A.; Wang, J.C.; Steinmetz, M.P.; Melillo, A.J.; Benzel, E.C.; Modic, M.T.; et al. Variability in surgical treatment of spondylolisthesis among spine surgeons. *World neurosurgery* **2018**, *111*, e564–e572.
24. Zubrzycki, J.; Smidova, N.; Litak, J.; Ausiyevich, A. Numerical Analysis of Spinal Loads in Spondylolisthesis Treatment using Pedicle Screws–Preliminary Research. *Applied Computer Science* **2017**, *13*.
25. Noh, H.; Hong, S.; Han, B. Learning deconvolution network for semantic segmentation. In Proceedings of the Proceedings of the IEEE international conference on computer vision, 2015, pp. 1520–1528.
26. Zhao, W.; Du, S.; Emery, W.J. Object-Based Convolutional Neural Network for High-Resolution Imagery Classification. *IEEE Journal of Selected Topics in Applied Earth Observations and Remote Sensing* **2017**, *10*, 3386–3396.
27. Iglovikov, V.; Seferbekov, S.; Buslaev, A.; Shvets, A. Ternausnetv2: Fully convolutional network for instance segmentation. In Proceedings of the Proceedings of the IEEE Conference on Computer Vision and Pattern Recognition Workshops, 2018, pp. 233–237.
28. Stoian, A.; Poulain, V.; Inglada, J.; Poughon, V.; Derksen, D. Land cover maps production with high resolution satellite image time series and convolutional neural networks: Adaptations and limits for operational systems. *Remote Sensing* **2019**, *11*, 1986.
29. Minaee, S.; Boykov, Y.; Porikli, F.; Plaza, A.; Kehtarnavaz, N.; Terzopoulos, D. Image Segmentation Using Deep Learning: A Survey. *CoRR* **2020**, *abs/2001.05566*.
30. Budd, S.; Robinson, E.; Kainz, B. A Survey on Active Learning and Human-in-the-Loop Deep Learning for Medical Image Analysis. *CoRR* **2019**, *abs/1910.02923*.
31. Litjens, G.; Kooi, T.; Bejnordi, B.E.; Setio, A.A.A.; Ciompi, F.; Ghafoorian, M.; Van Der Laak, J.A.; Van Ginneken, B.; Sánchez, C.I. A survey on deep learning in medical image analysis. *Medical image analysis* **2017**, *42*, 60–88.
32. Lecron, F.; Mahmoudi, S.A.; Benjelloun, M.; Mahmoudi, S.; Manneback, P. Heterogeneous Computing for Vertebra Detection and Segmentation in X-Ray Images. *Int. J. Biomed. Imaging* **2011**, *2011*, 640208:1–640208:12.
33. Ronneberger, O.; Fischer, P.; Brox, T. U-Net: Convolutional Networks for Biomedical Image Segmentation **2015**. *9351*, 234–241.
34. Kuok, C.; Fu, M.J.; Lin, C.J.; Horng, M.S.Y. Vertebrae Segmentation from X-ray Images Using Convolutional Neural Network. *Proceedings of the 2018 International Conference on Information Hiding and Image Processing* **2018**, pp. 57–61.
35. Konya, S.; Sai Natarajan, T.R.; Allouch, H.; Nahleh, K.A.; Dogheim, O.Y.; Boehm, H. Convolutional Neural Networks based automated segmentation and labelling of the lumbar spine X-ray. *CoRR* **2020**, *abs/2004.03364*.

36. He, K.; Gkioxari, G.; Dollár, P.; Girshick, R. Mask r-cnn. In Proceedings of the Proceedings of the IEEE international conference on computer vision, 2017, pp. 2961–2969.
37. Ren, S.; He, K.; Girshick, R.; Sun, J. Faster R-CNN: towards real-time object detection with region proposal networks. *IEEE transactions on pattern analysis and machine intelligence* **2016**, *39*, 1137–1149.
38. Zhao, H.; Shi, J.; Qi, X.; Wang, X.; Jia, J. Pyramid scene parsing network. In Proceedings of the Proceedings of the IEEE conference on computer vision and pattern recognition, 2017, pp. 2881–2890.
39. Chen, L.C.; Papandreou, G.; Schroff, F.; Adam, H. Rethinking atrous convolution for semantic image segmentation. *arXiv preprint arXiv:1706.05587* **2017**.
40. Bolya, D.; Zhou, C.; Xiao, F.; Lee, Y.J. Yolact: Real-time instance segmentation. In Proceedings of the Proceedings of the IEEE/CVF International Conference on Computer Vision, 2019, pp. 9157–9166.
41. Cho, B.; Kaji, D.; Cheung, Z.; Ye, I.B.; Tang, R.; Ahn, A.; Carrillo, O.; Schwartz, J.T.; Valliani, A.A.; Oermann, E.K.; et al. Automated Measurement of Lumbar Lordosis on Radiographs Using Machine Learning and Computer Vision. *Glob. Spine J.* **2019**, pp. 1–8.
42. Badrinarayanan, V.; Kendall, A.; Cipolla, R. SegNet: A Deep Convolutional Encoder-Decoder Architecture for Image Segmentation. *IEEE Transactions on Pattern Analysis and Machine Intelligence.* **2017**, *39*, 2481–2495.
43. Li, Z.; Zhou, F. FSSD: feature fusion single shot multibox detector. *arXiv preprint arXiv:1712.00960* **2017**.
44. Chen, L.; Papandreou, G.; Kokkinos, I.; Murphy, K.; Yuille, A.L. Semantic Image Segmentation with Deep Convolutional Nets and Fully Connected CRFs. *3rd International Conference on Learning Representations, ICLR* **2015**.
45. Yu, C.; Wang, J.; Peng, C.; Gao, C.; Yu, G.; Sang, N. Bisenet: Bilateral segmentation network for real-time semantic segmentation. In Proceedings of the Proceedings of the European conference on computer vision (ECCV), 2018, pp. 325–341.
46. Zhao, S.; Wu, X.; Chen, B.; Li, S. Automatic spondylolisthesis grading from MRIs across modalities using faster adversarial recognition network. *Medical image analysis* **2019**, *58*, 101533.
47. Ansari, S.; Sajjad, F.; Naveed, N.; Shafi, I.; et al. Diagnosis of vertebral column disorders using machine learning classifiers. In Proceedings of the 2013 International Conference on Information Science and Applications (ICISA). IEEE, 2013, pp. 1–6.
48. Karabulut, E.M.; Ibrikci, T. Effective automated prediction of vertebral column pathologies based on logistic model tree with SMOTE preprocessing. *Journal of medical systems* **2014**, *38*, 1–9.
49. Akben, S.B. Importance of the shape and orientation of the spine and pelvis for the vertebral column pathologies diagnosis with using machine learning methods. *Biomedical Research-India* **2016**, *27*, S337–S342.
50. Unal, Y.; Polat, K.; Kocer, H.E. Pairwise FCM based feature weighting for improved classification of vertebral column disorders. *Computers in biology and medicine* **2014**, *46*, 61–70.
51. da Rocha Neto, A.R.; de Alencar Barreto, G. On the application of ensembles of classifiers to the diagnosis of pathologies of the vertebral column: A comparative analysis. *IEEE Latin America Transactions* **2009**, *7*, 487–496.